Materials Chemistry and Physics 291 (2022) 126694

Contents lists available at ScienceDirect

Materials Chemistry and Physics

journal homepage: www.elsevier.com/locate/matchemphys

Mechanistic modelling of atmospheric corrosion of carbon steel in Port-Louis by electrochemical characterisation of rust layers

Yashwantraj Seechurn [a,b,*], Julian A. Wharton [a], Baboo Y.R. Surnam [b]

[a] National Centre of Advanced Tribology at Southampton (nCATS), School of Engineering, University of Southampton, Southampton, SO17 1BJ, UK
[b] Mechanical and Production Engineering Department, Faculty of Engineering, University of Mauritius, Reduit, 80837, Mauritius

HIGHLIGHTS

- Anodic dissolution at ferrite locations leads to porous rust layers.
- Large voids/cracks in a corrosion layer cause anomalous diffusion of reactants.
- Lepidocrocite is the predominant rust phase after 14 months regionwide.
- Rust layer resistance can be quantified with EIS performed in a simulant solution.
- Mountains and coastal bays have geospatial influence on chloride deposition rate.

ARTICLE INFO

Keywords:
Carbon steel
EIS
X-ray diffraction
Atmospheric corrosion
Rust

ABSTRACT

S235 structural steel was exposed for 14 months at six locations in the marine/urban atmosphere of Port-Louis, distinguished by the surrounding bay and mountains. An unusual geospatial variability in terms of chloride deposition rate (7.8–54.3 mg m^{-2} d^{-1}), SO_2 level (1.2–2.4 mg m^{-2} d^{-1}) and corrosion rate (77.6–189.2 g m^{-2} y^{-1}) was observed. Electrochemical techniques, supported by mass loss and surface analysis, provide insights into environment-specific corrosion mechanisms, with the occurrence of anomalous diffusion at the aggressive exposure sites. Rust layer corrosion resistances ranged between 4 and 113 Ω cm^2.

1. Introduction

Atmospheric corrosion is a complex phenomenon associated with a wide range of environmental factors combining in a specific manner with the corroding surface. Carbon steel brings its own variability in terms of the alloying elements present, leading to diverse corrosion products depending on humidity levels, concentration of pollutants such as sulphur dioxide (SO_2) and amount of marine aerosols in the atmosphere, all which vary geographically [1]. While atmospheric corrosion in the tropics have been widely researched for the western hemisphere [2–7], making corrosivity information widely accessible, such is not the case for the Indian Ocean island of Mauritius, possessing unique attributes due to atypical climate variability. This study aims to determine the corrosion mechanism (through an investigation of corrosion layers) in the coastal city of Port-Louis, characterised by its oil-fired power stations releasing SO_2 gases in the atmosphere and a complex distribution of chlorides (Cl^-) due to presence of a mountain range and a bay (Fig. 1).

Corrosion layers have an important role in defining the eventual rate of progression of corrosion depending on their protective ability [8]. The corrosion products/oxide phases are subject to specific transformation based on the prevailing environmental conditions [9]. Hydroxides or salts of the metal formed in neutral or acidic conditions, accumulate on the surface, and may gradually form a friable and porous layer, which is not effective in halting corrosion but may cause reduced metal dissolution. Such is the case for steel in a humid environment [10]. In a slightly acidic atmosphere, the pH has a noticeable influence on iron dissolution rate. According to Bockris, iron dissolution occurs in three stages (Eqns. (1)–(3)), starting with two consecutive one-electron exchange reaction steps [10]. The intermediate stage is the rate determining step, i.e., the process defining the corrosion rate. The adsorbed species, $FeOH_{ads}$, appears as the reaction intermediate, producing the observed pH dependency for the dissolution reaction.

---

[*] Corresponding author. Mechanical and Production Engineering Department, Faculty of Engineering, University of Mauritius, Reduit, 80837, Mauritius.
E-mail address: y.seechurn@uom.ac.mu (Y. Seechurn).

https://doi.org/10.1016/j.matchemphys.2022.126694
Received 25 April 2022; Received in revised form 9 August 2022; Accepted 20 August 2022

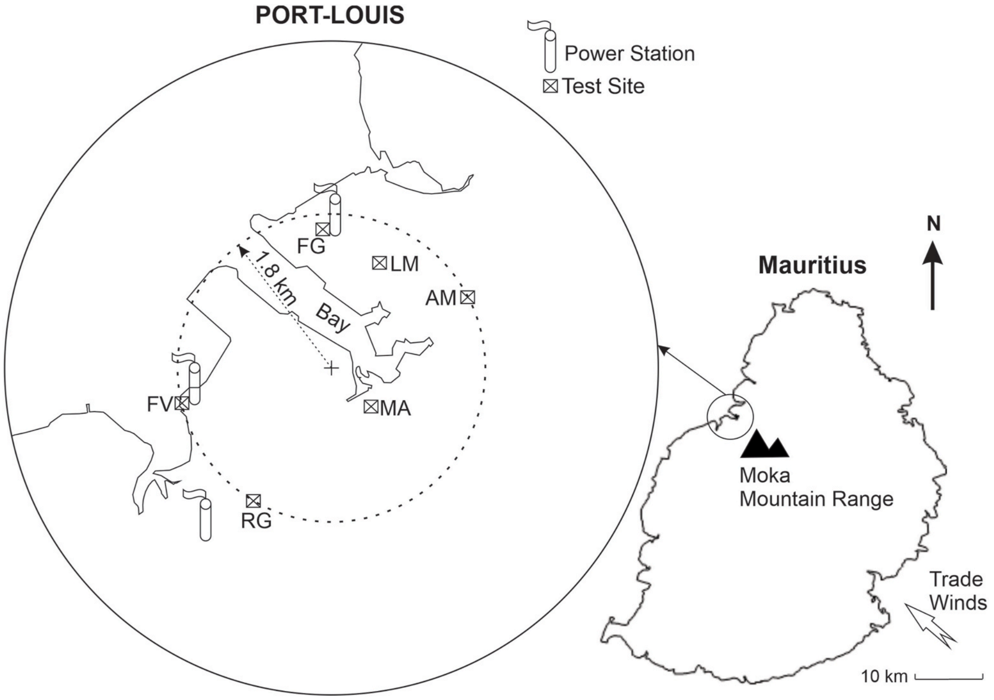

Fig. 1. Map of Port-Louis showing the various atmospheric exposure sites.

$$Fe + OH^{-} \rightarrow FeOH_{ads} + e^{-} \quad (1)$$

$$FeOH_{ads} \rightarrow FeOH^{+} + e^{-} \quad (2)$$

$$FeOH^{+} + H^{+} \rightarrow Fe^{2+} + H_2O \quad (3)$$

In some cases, the rate determining step is the oxygen reduction reaction which requires oxygen from the air to diffuse through a water layer (condensation films) and any corrosion products to reach the metal substrate. The thickness of such surface layers plays a major role in defining diffusion processes [11]. Progression of the atmospheric corrosion mechanism may therefore depend on the oxide phases formed, which differ according to the environmental conditions. For example, high humidity and a less adherent corrosion product layer facilitate diffusion of oxygen through the corrosion products. Furthermore, the cathodic kinetics depend on the additional thickness of electrolyte film on the metal surface, which increases and decreases during the alternating wet and dry conditions, respectively. The latter causes the potential of the metal to vary periodically. The corrosion potential shifts electropositively due to the formation of surface rust layers [12]. Growth of corrosion products increase the surface area of the metal and the volume of material affected in a wet cycle. Consequently, the aqueous condition is prolonged, and corrosion is more pronounced due to its electrochemical nature.

Electrochemical techniques offer the possibility of tracking a degradation process from beginning to end, albeit at discrete time intervals. However, the study of electrochemical processes involving rusted steel is complex [13]. Such techniques are not widely accepted as a means for characterisation of corrosion product layers. It is possible that data computed for such simulated experiment give a lower corrosion rate than using the output of mass-loss analysis, especially in the presence of chemical reactions other than those modelled by the electrochemical cell [14]. Deliquescence of sodium chloride (NaCl), which is often used in simulated/accelerated exposure tests, stimulates corrosion at a higher relative humidity level than in the presence of naturally occurring salts [15]. The latter are predominant in marine atmospheres due to the presence sea salt droplets/particles of differing Deliquescent Relative Humidity (DRH), mainly NaCl and magnesium chloride ($MgCl_2$), with the former in higher proportion. Condensation of NaCl occurs in atmospheres having RH greater than 75% (DRH of NaCl) while condensation of $MgCl_2$ is triggered above an RH of 35% (DRH for $MgCl_2$) [16]. Nevertheless, the rust layer has electrochemical activity, such as the semiconducting magnetite phase, which allows interfacial movement of electrons and metal ions, and therefore electrochemical measurements would be very effective in studying corrosion mechanisms, including the ability of the corrosion layer to act as a barrier to further degradation [17].

Corrosion damage (M) *vs.* time (t) is generally known to follow a power law relationship in the form of $M = At^n$, where constants A and n give an indication of the corrosivity of the atmosphere and protectiveness of the rust layer respectively [18]. However, linear regression to fit the power law has proved to be inadequate in achieving a detailed understanding of the corrosion kinetics of a specific material [8]. Electrochemical measurement is an established rapid technique to validate the corrosion behaviour of the bare or rust covered metal by immersion in a representative solution. In coastal regions, corrosion is heavily influenced by the chloride deposition rate on metallic surfaces covered with condensation films. Electrochemical tests in either artificial seawater or simplified chloride media is a means to study the interaction of chloride ions with a corroded metal in a wetted condition [19]. This is an instantaneous measurement, especially in comparison to field exposure. Such an experiment requires the specimen to have an adherent/consolidated rust layer, *i.e.*, there should be use of samples which have not been exposed to highly corrosive atmospheres whereby exfoliation causes the outer layer to undergo cracking due to penetration of chloride ions. The current study demonstrates the underlying carbon steel corrosion mechanism based on electrochemical tests carried out on specimens exposed at six locations in a tropical humid urban/marine atmosphere of varied atmospheric conditions within a 1.8 km radius, depending on distance from seashore or anthropogenic pollution sources.

Table 1
Chemical composition of S235 structural carbon steel.

Elements	C	Mn	P	S	Si	Cu
Composition (wt%)	0.17	1.4	0.04	0.04	0.05	0.55

Table 2
Elevation and distance of the exposure sites from the seashore and power plants.

Site	AM	LM	MA	RG	FV	FG
Elevation/m	12	4	11	41	6	8
Distance from seashore/m	620	750	203	200	16	350
Distance from power plant/m	1770	700	2100	680	43	50

2. Materials and methods

2.1. *Atmospheric exposure*

Port-Louis (20.2°S 57.3°E) is the largest city situated on the north-west coast of Mauritius, comprising of the harbour and three heavy oil-fired power stations (Fig. 1). The island is found in the Indian Ocean, 2000 km on the east coast of Africa and has a tropical climate. Mauritius experiences two seasons: winter and summer, with a high humidity throughout the year, up to 86% in the highlands and to a lesser extent in coastal areas [20]. The mean annual temperature determined from data between 1971 and 2000 is 22 °C [21]. For the same period, the mean annual rainfall is 2100 mm with the summer months of January till March being the wettest [21]. To determine the corrosion behaviour of bare carbon steel, S235 (EN 10025 S235JR) structural steel plates (size: 150 mm × 100 mm × 3 mm) of composition shown in Table 1 were exposed to the atmosphere at six sites in the city as shown in Fig. 1: ABC Motors (AM), Fort George (FG), Fort Victoria (FV), Landscope Mauritius (LM), Mutual Aid (MA) and Rajiv Gandhi Science Centre (RG). The exposure sites were chosen taking into consideration their proximity with the seashore and/or power station (Table 2).

The Cl^- deposition rate was determined using the Wet Candle method and the SO_2 concentration in the atmosphere was obtained from analysis of lead oxide sulfation plates placed at each exposure location [22]. The steel plates were cleaned with 10% wt./vol. HCl and stored under dry conditions in a desiccator until exposure [23]. The plates were installed at 45° to the horizontal, on racks facing the ocean. As shown in Fig. 2, the accessories for measurement of Cl^- and SO_2 were set up with the rack. Five plates (three for weight loss analysis plus one each for surface analysis and electrochemical characterisation) were removed at each exposure timepoint of two, five, eight, 11- and 14-months. With the exception for LM at 11-months when the retrieval was hindered due to site inaccessibility at that timepoint.

2.2. *Weight-loss analysis*

For each collection at a specific site, the Kern precision balance PB 400-3 was used to measure the mass of each of the plates, to three decimal places, following removal of corrosion products by immersion in 50% wt./vol. HCl, with 3.5 g L^{-1} hexamethylenetetramine [24]. ISO 9223 was used to characterise the corrosivity of each atmospheric test site based on the corrosion rate [22]. The latter, calculated as per Eqn. (4) [25] also allowed assessment of the corrosion damage expressed by Eqn. (5) [26].

$$r_{\mathrm{corr}} = \frac{\Delta m}{A \cdot t} \qquad 4$$

where r_{corr} is the corrosion rate in g m^{-2} y^{-1}, Δm is the mass loss in g, A is the surface area in m^2, t is the exposure time in years (y),

$$D = r_{\mathrm{corr}} t^{b} \qquad 5$$

where D is the total attack in g m^{-2} and b is a time exponent parameter that is indicative of the metal and environment.

2.3. *Surface analysis using XRD and SEM*

A representative internal area of 40 mm × 40 mm, cut from each plate, was taken for surface analysis with the Zeiss Merlin Scanning Electron Microscope used for morphological examination, and the Rigaku Smartlab X-Ray diffractometer for oxide phase identification. Equipped with a 9 kW (45 kV, 200 mA) Cu rotating anode source and a one-dimensional silicon strip detector, the diffractometer was set up to operate for a scan range between 10° and 60°, at a step width of 0.03° and a scan speed of 3 deg. min^{-1}. Identification of the various crystalline compounds in each sample was then carried out by comparing the diffraction patterns to a database containing reference patterns.

2.4. *Electrochemical characterisation*

A Gamry Reference 600 potentiostat with Gamry Framework version 6.33 data acquisition software were used to perform potentiodynamic polarization and electrochemical impedance spectroscopy (EIS) on the as-prepared/unexposed and atmospherically corroded carbon steel plates to determine the properties of the corrosion product layers after

Fig. 2. Atmospheric corrosion exposure set-up for field tests.

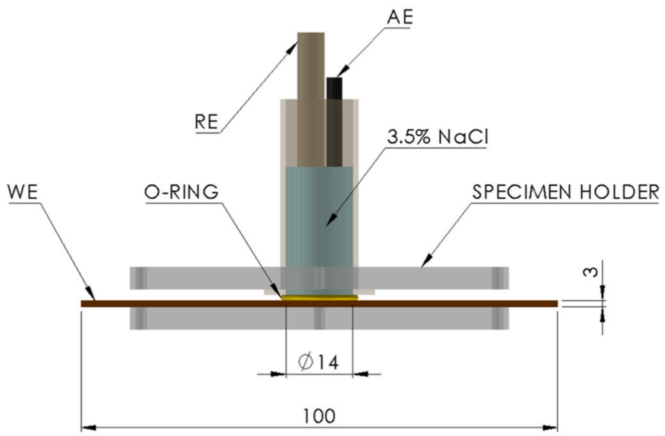

Fig. 3. Electrochemical test set-up post atmospheric exposures with intact corrosion product layers (dimensions in mm).

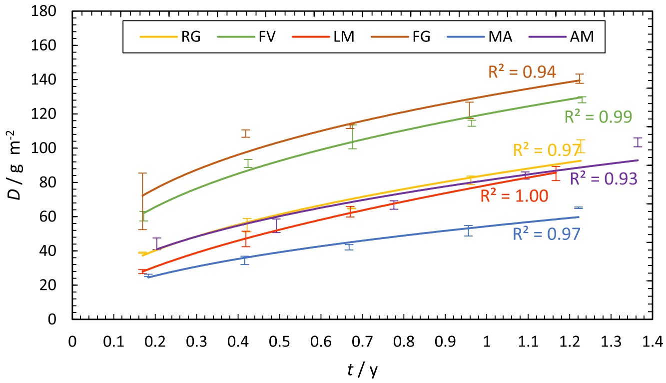

Fig. 4. Atmospheric corrosion of S235 structural carbon steel *vs.* time at the six exposure locations within Port-Louis, Mauritius (marine/urban environmental conditions): (a) AM, (b) LM, (c) MA, (d) RG, (e) FG and (f) FV.

two, five, eight, 11- and 14-months exposure. Potentiodynamic polarization can provide an approximation of the corrosion rate while EIS is a useful method to study the underlying corrosion mechanisms [27,28]. All experiments were conducted within a Faraday cage. An electrode cell as shown in Fig. 3 was used to hold a rectangular plate in position with an exposed area of 1.54 cm^2. A silver/silver chloride (Ag/AgCl) reference electrode (RE) and a platinum auxiliary electrode (AE) were used. The working electrode (WE) was immersed in a 3.5 wt% NaCl test solution of pH 6.65 and DO 8.15 mg/L for 1 h to assess the open-circuit potential (OCP). EIS was performed at a pseudo steady-state open-circuit potential using an AC voltage of ±10 mV and a frequency range between 10^5 Hz and 10^{-2} Hz. Finally, a potentiodynamic polarization, between −0.250 V and +0.250 V with respect to the corrosion potential, was applied at a sweep rate of 0.33 mV s^{-1}. Experiments were performed in triplicate.

3. Results and discussion

3.1. Atmospheric corrosion tests

Table 3
Atmospheric pollution data and Corrosion Progression assessment for the six exposure sites.

Test Site	Cl$^-$ level/ mg m^{-2} d^{-1}	SO$_2$ level/ mg m^{-2} d^{-1}	Power-law expressions (*b* exponent)	11–months r_{corr}/ g m^{-2} y^{-1}
FV	26.05	2.37	$D = 120.02t^{0.38}$	170.2
RG	54.29	1.43	$D = 84.299t^{0.46}$	121.0
FG	29.51	1.90	$D = 130.44t^{0.33}$	189.2
MA	7.76	1.36	$D = 54.362t^{0.47}$	77.6
AM	26.99	1.39	$D = 77.175t^{0.43}$	114.2
LM	12.07	1.16	$D = 78.342t^{0.58}$	104.6

Generally, atmospheric corrosion product layers on steel tend to be moderately protective, thus the corrosion rate decreases with time and achieves a steady-state/uniform condition within a few years [1]. The degree of compactness (non-porosity) of the corrosion layer formed usually determines the extent to which the corrosion kinetics are affected [29]. Higher corrosion rates are typically reported in marine and industrial atmospheres indicating that the corrosion products formed in these atmospheres are less protective. In this study, the corrosion-time curves (Fig. 4) follow a power-law function with the high R^2 values showing a good fit. The individual power-law expression and atmospheric contaminants measured at the test sites are listed in Table 3. The shape of the plots, of the form $M = At^n$, is similar to that obtained from data of previous studies [1]. However, typical plots for marine atmospheres usually have much higher values of n, while in this instance all test sites display n values lower than or around 0.5. Nevertheless, Fig. 4 clearly demonstrates that the corrosion damage is significantly higher for FV and FG compared to the other exposure locations.

The deposition rates of Cl$^-$ and SO$_2$ are monthly measurement averages taken at four time points during the exposure period (two per season – winter and summer). A general observation is the low SO$_2$ pollution level of P_0 category ($P \leq 4$ mg m^{-2} d^{-1}), which is representative of a rural atmosphere [22], regionwide. However, there is still an appreciable difference between the SO$_2$ levels. The two highest SO$_2$ values occur at FV and FG linked to the proximity of these two locations to power plants releasing SO$_2$ gases in the atmosphere. The Cl$^-$ deposition rates are all within the S_1 category (3 mg m^{-2} d^{-1} $< S \leq 60$ mg m^{-2} d^{-1}) [22], which is low for a marine atmosphere, most likely due to the regular wash-off of any deposited marine salts in a region with a high frequency of precipitation. The salinity at RG is almost double than that found at FV, FG and AM, whilst LM and MA have markedly lower salinities. MA is much closer to the seashore than LM, however waves tend to be smaller in bays [30], which may not generate significant marine aerosol. Time-of-Wetness (TOW), considered as an environmental factor in atmospheric corrosion studies [31] and defined as the period during which relative humidity (RH) exceeds 80% with a temperature above 0 °C [22], was estimated at 1798 h using the daily variation of RH [32]. RH varies throughout the year, and this was taken into consideration when calculating the number of hours surfaces remain wet. The monthly averages of RH, temperature and amount of rainfall in Port-Louis are 69%, 26.0 °C and 93 mm, respectively [33]. The RH being less that the DRH for NaCl implies deliquescence of chloride is mainly from MgCl$_2$, which occurs in minor proportions of marine aerosols.

The corrosion rates for the first year of exposure, approximated in this study by considering the results from the 11-months exposed samples (Table 3), all lie in the low corrosivity category C2 ($10 < C \leq 200$ g m^{-2} y^{-1}), with those at FV and FG very close to C3 ($200 < C \leq 400$ g m^{-2} y^{-1}) and significantly lower values at the other locations [22]. This provides good corroboration with the pollutant level since the highest corrosion rates occur closer to the power plants and airborne salinity is having a pronounced effect at the sites further away with inferior amounts of SO$_2$ in the atmosphere. Furthermore, from Fig. 4 the exponent *b* shows that although higher amount of SO$_2$ for a particular site gives a high initial corrosion rate, a more protective corrosion product layer is formed with time [2]. Similar one-year corrosion rates were reported for AISI-SAE plain steel exposed to the urban/industrial atmospheric conditions of Bogota (Columbia). The corrosivity classification of the various sites were obtained as C2 and C3, with the city having many strategic locations of varying environmental conditions [34].

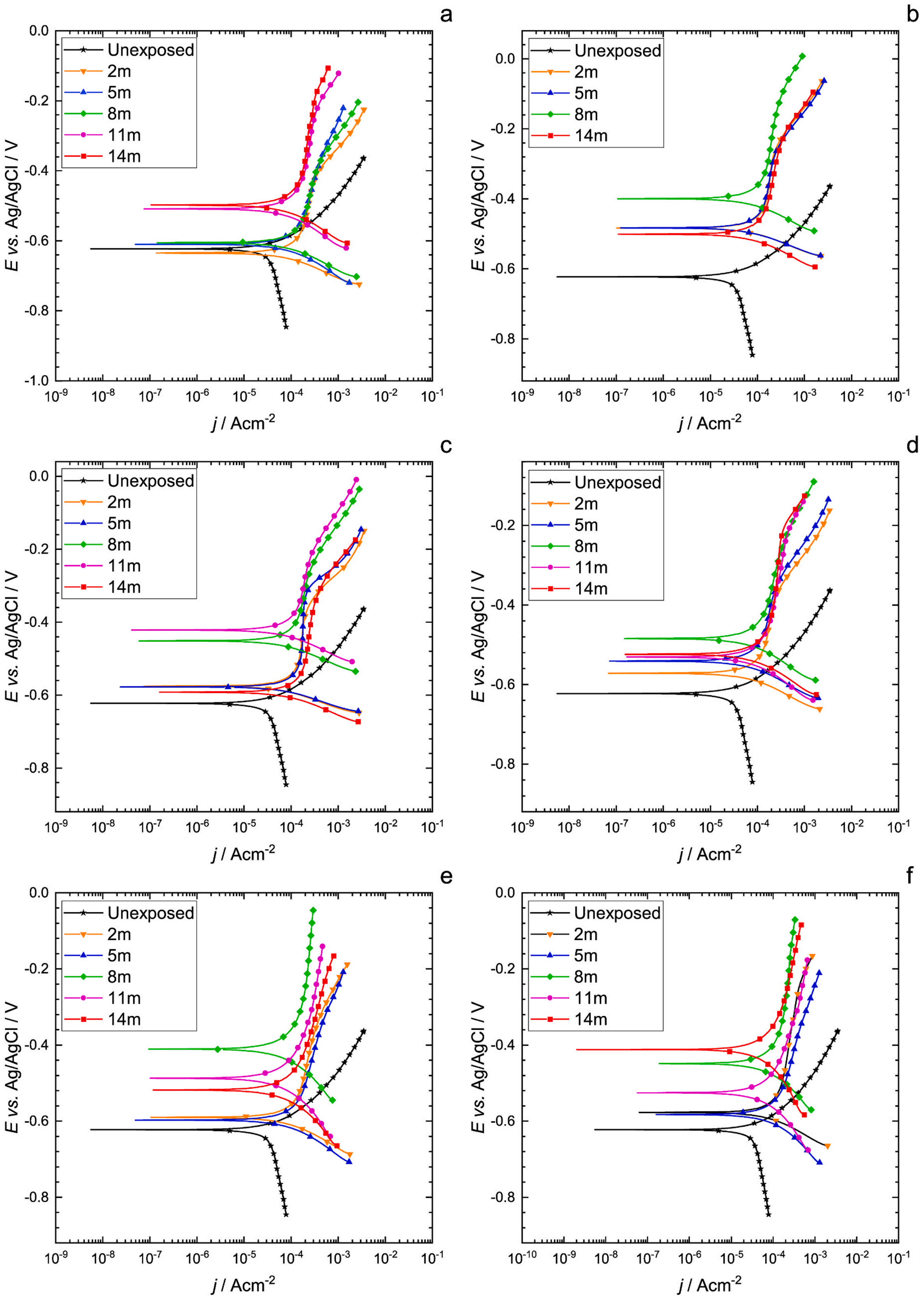

Fig. 5. Potentiodynamic polarizations of unexposed and corroded S235 carbon steel in 3.5 wt% NaCl solution after atmospheric exposure at locations: **(a)** AM, **(b)** LM, **(c)** MA, **(d)** RG, **(e)** FG, and **(f)** FV.

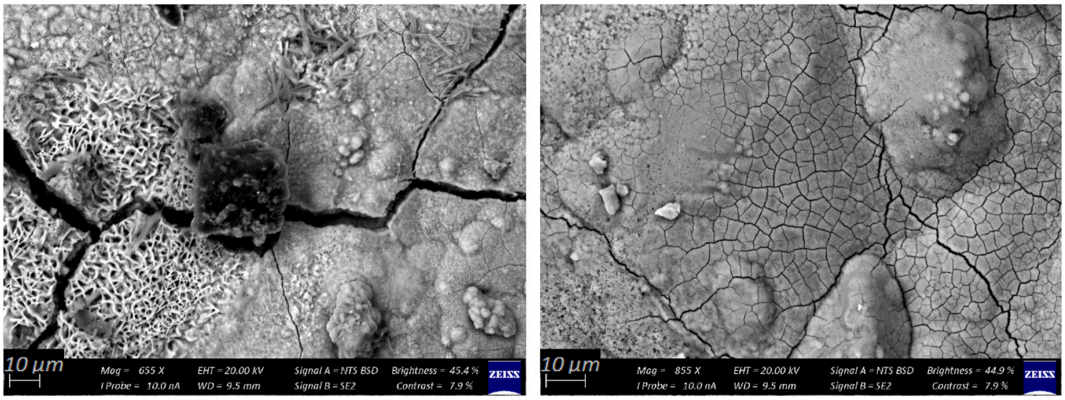

Fig. 6. SEM image of cracks observed on the corroded S235 carbon steel surface after 11 months of exposure at FG (left) and MA (right).

3.2. Ex situ electrochemical characterisation (post atmospheric exposure)

3.2.1. Potentiodynamic polarization

It is known that the atmospheric corrosion resistance of a layer of corrosion products can be assessed by its anodic polarization performance [9]. Potentiodynamic polarization was initially carried out for the as prepared/unexposed S235 steel in a 3.5 wt% NaCl electrolyte (Fig. 5), to establish a benchmark. The potentiodynamic polarization shows a mixed potential (often referred to as the corrosion potential, E_{corr}) of around −0.625 V and a corrosion current density (j_{corr}) of approximately 35 μA cm^{-2}. The redox potential for a natural atmosphere, being slightly acidic, is lower and in the range between 0.3 V and 0.5 V [18]. The predominant anodic and cathodic reactions are iron dissolution (Eqn. (6)) and oxygen reduction (Eqn. (7)).

$$Fe \rightarrow Fe^{2+} + 2e^{-} \qquad 6$$

$$O_2 + 2H_2O + 4e^{-} \rightarrow 4OH^{-} \qquad 7$$

The anodic reaction involving metal ion dissolution is not only accompanied by cathodic reduction of oxygen, but there are several other processes which could potentially occur, such as reduction of the corrosion products formed, movement of electroactive species through the rust layer, etc. Compared to unexposed steel, the cathodic kinetics as displayed by the potentiodynamic polarizations in Fig. 5, are much higher for the corroded samples. Cathodic curves for the latter are associated with the reduction of corrosion products in addition to oxygen reduction [35], indicating a different corrosion mechanism for rusted carbon steel. Corrosion product layers usually act as a physical barrier, which reduces exposure of the electrolyte to the underlying metal surface and therefore reduces the rate of metal dissolution. This also explains the positive shift of the open-circuit potential up to at least eight months' exposure, caused by a thicker oxide layer [36]. Therefore, better corrosion protection is achieved with formation of the oxide layer [37], limiting the charge transfer process at the metallic interface. A further increase in open-circuit potential at 11 months for MA can be explained by a relatively compact layer existing for a longer time at this site, with surface cracks beginning to increase in size in the corrosion layer at the other sites, such as FG, as shown in Fig. 6. Cracks observed from SEM images of 11-months exposed specimens at FG and MA confirm the existence of a porous surface layer at these sites, although use of ultra-high vacuum SEM may have contributed to open the cracks slightly further.

The potentiodynamic polarizations for AM, MA, LM and RG, illustrated in Fig. 5, do not show any significant change in the cathodic behaviour which means that the amount of lepidocrocite (λ-FeOOH) rust phase undergoing reduction remained constant [35]. Fig. 7 shows the SEM of corroded surfaces from these exposure locations, which clearly indicate the presence of γ-FeOOH in various morphologies. λ-FeOOH is also expected to be predominant after two months of exposure at FV and FG. However, FV displays a significant decrease in cathodic kinetics from two months to five months. FV is closer in distance to both the seashore and a power station than any other sites in Port-Louis. The same effect, but to a smaller extent, is observed at FG. The magnetite (Fe_3O_4) phase, present in an inner conducting layer formed from λ-FeOOH reduction [18], usually provides a cathodic surface allowing more oxygen to be reduced [10]. However, λ-FeOOH is preferentially transformed into goethite (α-FeOOH) instead of Fe_3O_4 in atmospheres with significant SO_2 content [38]. This is observed by SEM (Fig. 8) and the XRD spectra of samples exposed for 14 months at FV and FG (Fig. 9), showing α-FeOOH in addition to the main rust phase (λ-FeOOH). Therefore, cathodic sites are only present on the outer layers, thus limiting oxygen diffusion reaching the underlying metallic surface as the rust layers grow thicker.

Changes in corrosion current density are usually associated with a development in the structure of the rust layer [35]. For all sites, except AM, the main change in anodic reaction rate occurs from five months to eight months, which represents a general decrease in corrosion rate possibly occurring due to formation of the less soluble goethite rust phase [39]. Two distinct shapes of the anodic curve, representing a fast corrosion stage (beginning) and a slow corrosion stage (end), indicate a transition period in the corrosion process.

3.2.2. Electrochemical impedance spectroscopy

The underlying physicochemical processes at the metal|oxide|solution interface include charge transfer, interfacial capacitance (charge storage) and diffusion components (mass transfer), and their coexistence in combinations to account for complex behaviour. The EIS data for the unexposed specimen are presented in a Nyquist plot (Fig. 10), which shows a capacitive loop at high frequency and an inductive loop in the low frequency region, both appearing in the negative imaginary plane. The depressed semi-circle form of the capacitive loop indicates charge transfer at the metal|electrolyte interface as a non-ideal capacitance, usually represented by a constant phase element (CPE) in an equivalent circuit [40]. The low frequency feature, as an inductive loop, does not have considerable effect on the electrochemical system as inductance is only dominant at high frequencies. Following adsorption of FeOH species ($FeOH_{ads}$) on the metal surface (Eqn. (1)), $FeOH_{ads}$ is transformed to $FeOH^{+}$ in the rate-determining step (Eqn (2)). At low frequencies, Eqn. (1) becomes the predominant reaction due to change of the surface potential with prolonged anode and cathode limits, resulting in accumulation of $FeOH_{ads}$ at the reaction sites. This causes the resistance for the rate determining step to decrease due to increased availability of $FeOH_{ads}$ to be transformed to $FeOH^{+}/Fe^{2+}$, leading to a low frequency hook [41].

The Bode phase angle plot (*θ vs. f*) for the unexposed specimen, in Fig. 11, shows the phase angle changing from 0° to −55° and then

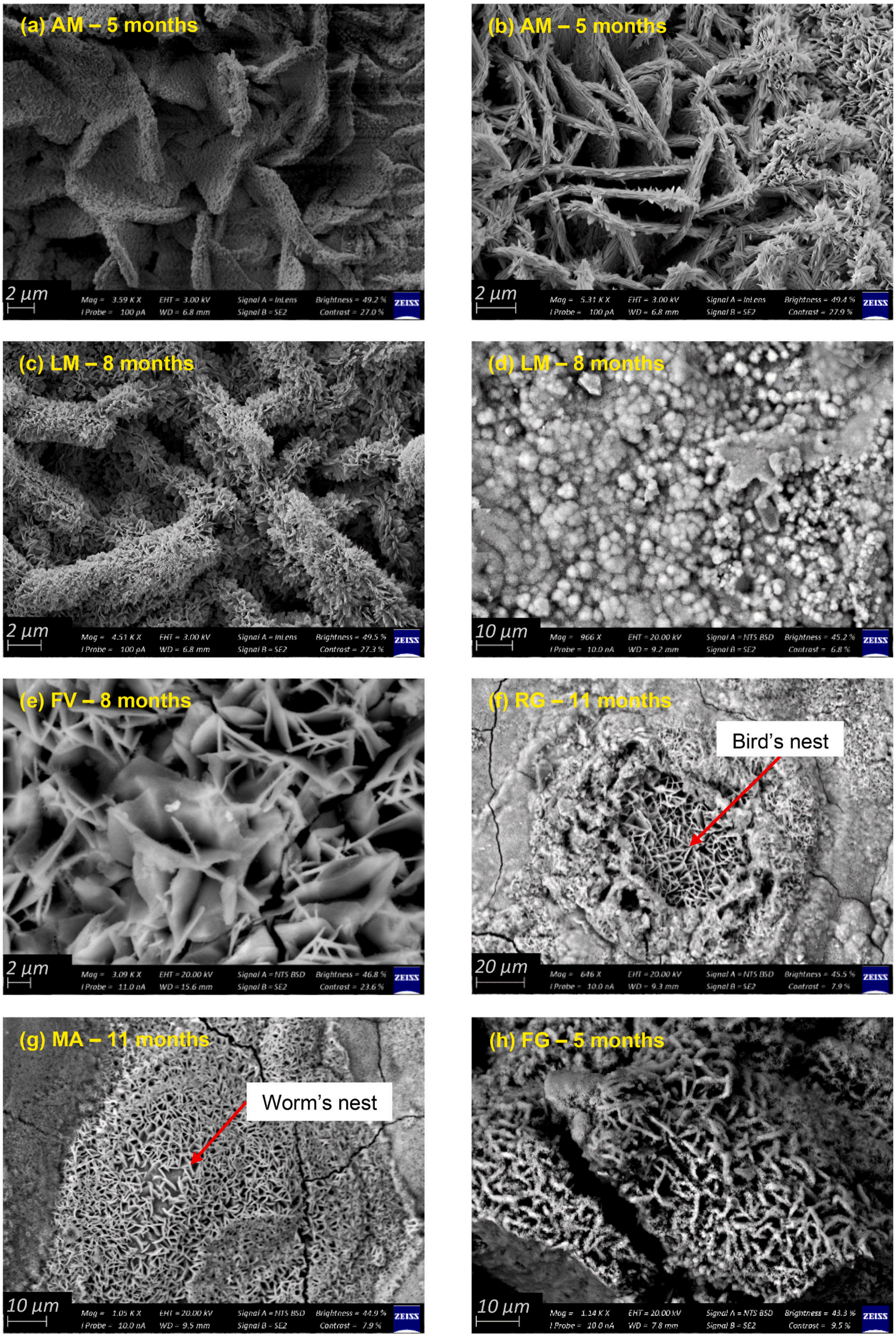

Fig. 7. λ-FeOOH morphologies observed at all locations: **(a, b)** laminas in the form of tree roots/tentacles, **(c)** bar-shaped laminas with a crystalline substructure, **(d)** sandy grains, **(e, f)** bird's nest, **(g, h)** laminar worm's nest.

returning close to 0° with increasing frequency. Overall, the system can be modelled using a simplified Randles cell (shown in the Appendix), with a constant phase element for the double layer capacitance (CPE_{dl}), whereby the current flows through a charge transfer resistance (R_{ct}) at low frequency due to high impedance of the capacitor (current chooses the path with the lowest impedance). As the frequency is increased and the impedance of the capacitor decreases, current will change path leading to a shift in phase angle. The Bode $|Z|$ plot for the unexposed specimen (Fig. 11) shows that increase in frequency causes a very low impedance such that the resistance of the solution (R_{s}) becomes more

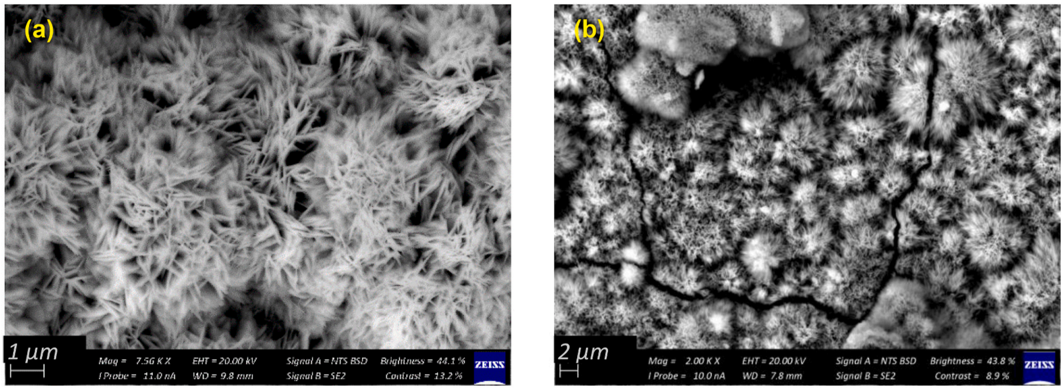

Fig. 8. α-FeOOH morphologies: **(a)** whiskers on eight-months exposed plate at FV and **(b)** thin straight sharp laminas on five-months exposed plate at FG.

significant. Results obtained from fitting of the equivalent circuit are given in the Appendix. n_{CPE} is 0.82, which implies a predominantly capacitive behaviour and a highly homogeneous surface [42].

As shown in Fig. 10, the Nyquist plots for almost all corroded plates subjected to increasing exposure periods at AM, LM, MA and RG show a straight diagonal line close to 45° at low frequency, implying the occurrence of Warburg diffusion [43]. A steeper line for the two-months and five-months exposed plates at MA suggests little corrosion while a lower slope of the low frequency part of the Nyquist plot, obtained from EIS of samples exposed at FV and FG (Fig. 10), indicates more corrosion [44]. The slope is generally reduced in the final stages of exposure indicating a change in porosity level pertaining to the nature of the oxide film formed at these locations.

In the absence of a double capacitive loop in all Nyquist plots, the corrosion process can be associated to a porous layer mechanism [44]. The charge transfer resistance is very low in the initial stages of exposure, with a prominence of Warburg impedance. Due to depletion of reduced species on the electrode surface, there is a decrease in current, and consequently there is mass transfer (diffusion) of oxygen (O_2) or hydroxide anions (OH^-) to and from the surface to compensate for the deficiency. This phenomenon is also associated to higher ions mobility at low frequencies [29]. Since the permeable corrosion layer is not effective as a barrier, the migration of species is eased, causing an acceleration of corrosion. This means that charge transfer occurs readily and diffusion impedance is the rate-determining process [44]. However, there is general progressive increase in size of the capacitive arc with time, which relates to the formation of a thicker rust layer. This leads to a hindering of the corrosion processes as contact of the electrolyte with the metal surface is significantly reduced.

The EIS Bode $-\theta$ plots (Fig. 11) give an approximately 10°–30° phase angle at low frequency (indicative of Warburg impedance), that tends towards 0° for the first few months of exposure, implying that the main impedance component at high frequency for this period is the rust layer resistance, occurring due to the mass transfer through the fine pores within the corrosion products [45]. The growth of the corrosion layer is also associated with an increase in Warburg impedance with time due to free diffusing species such as oxygen having to travel longer distances as it diffuses through the rust layer. For the first two removals, as shown in the EIS Bode θ plots, the system reaches nearly full resistive behaviour as frequency increases. However, later during exposure, there seems to be a tendency for deviation from 0°, which means that the rust layer resistance no longer dominates. The EIS Bode $|Z|$ plots for two and five months (Fig. 11) confirm that the impedance at high frequency in the early stages is clearly the resistive component as shown by the gradual decrease of $|Z|$ to a steady value. Furthermore, the high frequency impedance values for the curves representing the initial stages of exposure (at least up to five months) are similar. For later stages, increasing capacitive characteristics are observed in Bode θ plots at high frequency. With time, an increase in thickness of the porous rust layer will create a longer channel for ions to flow, thus causing a general increase in impedance as shown in the Bode $|Z|$ plots. However, the high frequency impedance at 14 months does not follow this trend, most probably due to formation of cracks leading to less resistance for migration of reactants. The corrosion layer becomes inefficient in slowing down the progress of corrosion due to its pervious nature [43].

Overall, the low frequency limit of impedance is lower at MA, indicating relatively slow growth of the rust layer for the whole exposure period at this location. A capacitive characteristic at high frequency is only seen for the 14-months exposed plate (from the Bode θ plot). However, the length of the diffusion tail in the Nyquist plot does not change significantly at 14 months. For AM and LM, the low frequency limits of impedance are significantly higher for the longer periods compared to the shorter periods, indicating presence of a thicker corrosion layer beyond eight or 11 months. The shape and size of the Nyquist and Bode plots for two and five months at AM, LM and MA are almost similar, indicating no marked change in the characteristics of the rust layer until at least five months. In contrast, the oxide film at RG evolves in a progressive manner with time. This is most probably due to the significantly higher chloride deposition rate at this site (around twice the rate measured at the other locations). The exchange current density, a measure of the corrosion rate, is generally higher with predominance of hydroxide ions on the metal surface [46]. However, presence of both chloride and hydroxide ions leads to a more aggressive environment for corrosion. Fig. 12 shows the interaction of ionic species on the wet metal surface subjected to sea salts deposition. On reaching the wet steel surface, the salt particles dissolve in the thin film of water and the adsorbed iron hydroxide ($\mathrm{FeOH_{ads}}$) develops into a specific surface complex ($\mathrm{FeOHCl^-_{ads}}$), which drives the anodic dissolution process (Eqns. (8) to (10)) [46]. Chloride usually penetrates the porous layer to form intermediate phases at the metal|rust interface, which then slowly transform into more stable and compact phases resulting in an adherent rust layer. However, a reduced chloride deposition rate due to the plates being exposed downwind and the wash-off effect of chlorides due to rainfall hinder the formation of iron oxychloride (FeClO), as shown from the XRD spectrum in Fig. 9. There is predominance of the soluble lepidocrocite rust phase across all locations after 14 months. The stable goethite phase, obtained from the reduction of lepidocrocite, decreases with time and the corrosion rate is expected to increase again. Fig. 9 also shows the presence of ferrous sulphates such as jarosite and rozenite (albeit in minor proportions).

$$\mathrm{FeOH_{ads}} + \mathrm{Cl^-} \rightarrow \mathrm{FeOHCl^-_{ads}} \tag{8}$$

$$\mathrm{FeOHCl^-_{ads}} \rightarrow \mathrm{FeOHCl_{ads}} + e^- \quad \text{(rate − determining step)} \tag{9}$$

$$\mathrm{FeOHCl_{ads}} + H^+ \rightarrow Fe^{2+} + Cl^- + H_2O \tag{10}$$

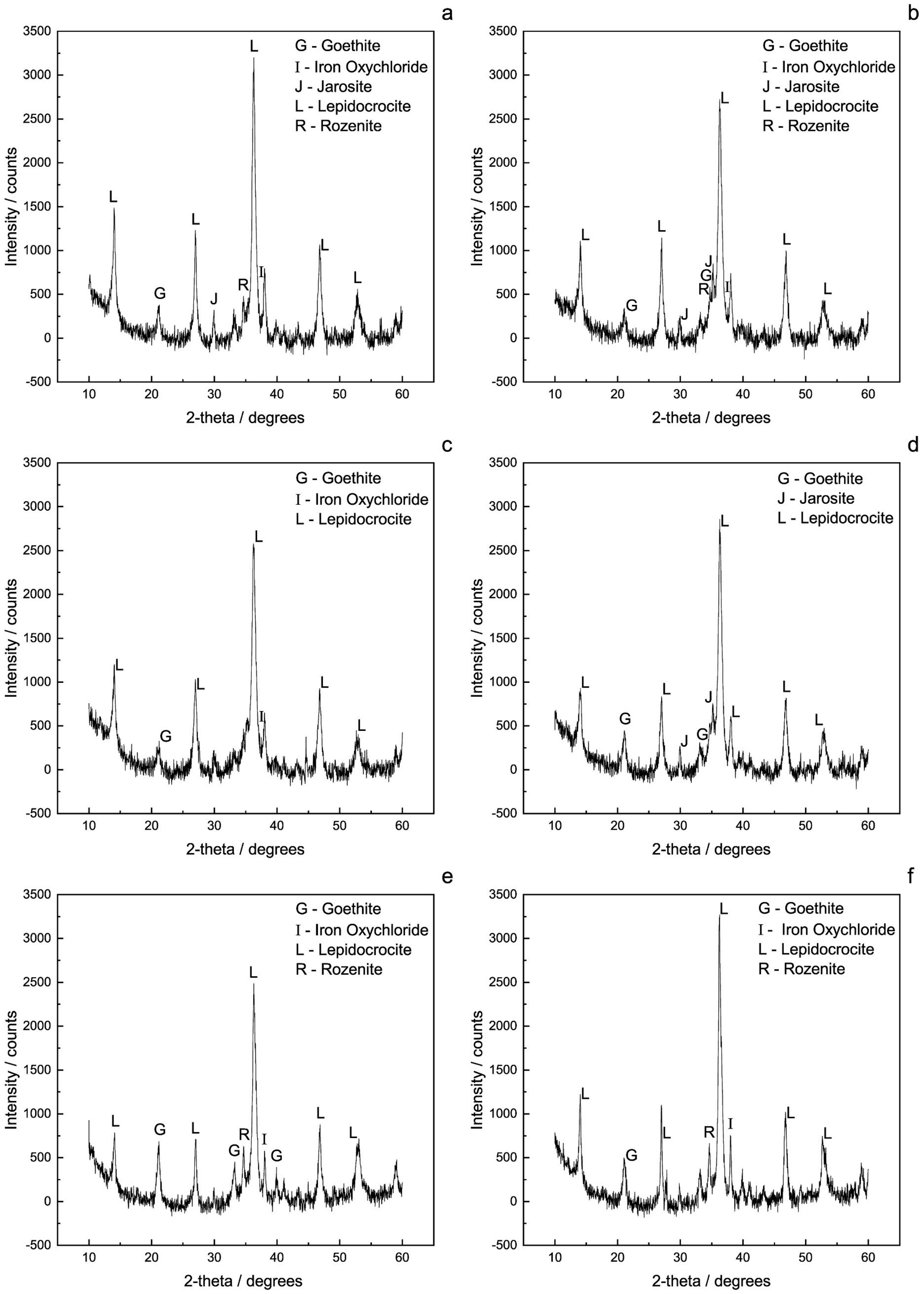

Fig. 9. XRD spectrum for 14-months exposed S235 carbon steel samples at locations: **(a)** AM, **(b)** LM, **(c)** MA, **(d)** RG, **(e)** FG and **(f)** FV.

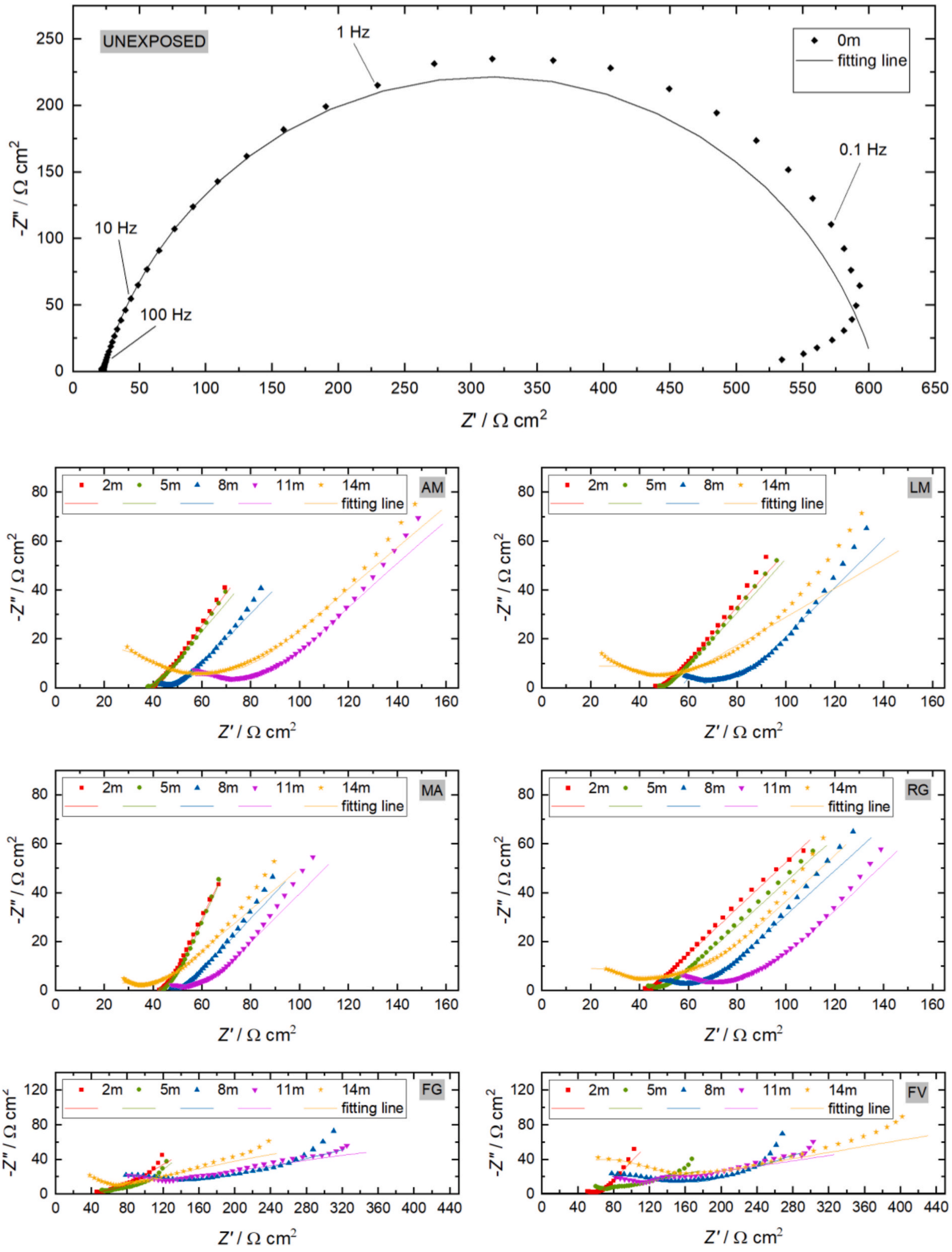

Fig. 10. Nyquist plots at OCP for the unexposed, and corroded S235 carbon steel after exposure at AM, LM, MA, RG, FG and FV in a 3.5 wt% NaCl solution.

With the exception of the two-months exposed sample at FV, the angle the low frequency curve makes with the real axis in the Nyquist plots for FV and FG is significantly below 45°, indicating a CPE behaviour due to non-uniform surface reactivity [47] and a porous surface with semi-infinite behaviour [48]. Given the relatively high SO_2 deposition on the metal surfaces at FV and FG (Table 3), there is an initial rapid corrosion at the beginning of exposure. Even after the metal is covered with an oxide or hydroxide layer, the atmospheric pollutants can permeate through the pores within the rust layer. Fig. 13 shows the rust structure of the cross-section at FG, obtained from optical imaging of an internal area of the 14-months exposed plate mounted in Bakelite.

Since the diffusion impedance feature is influenced by the thickness

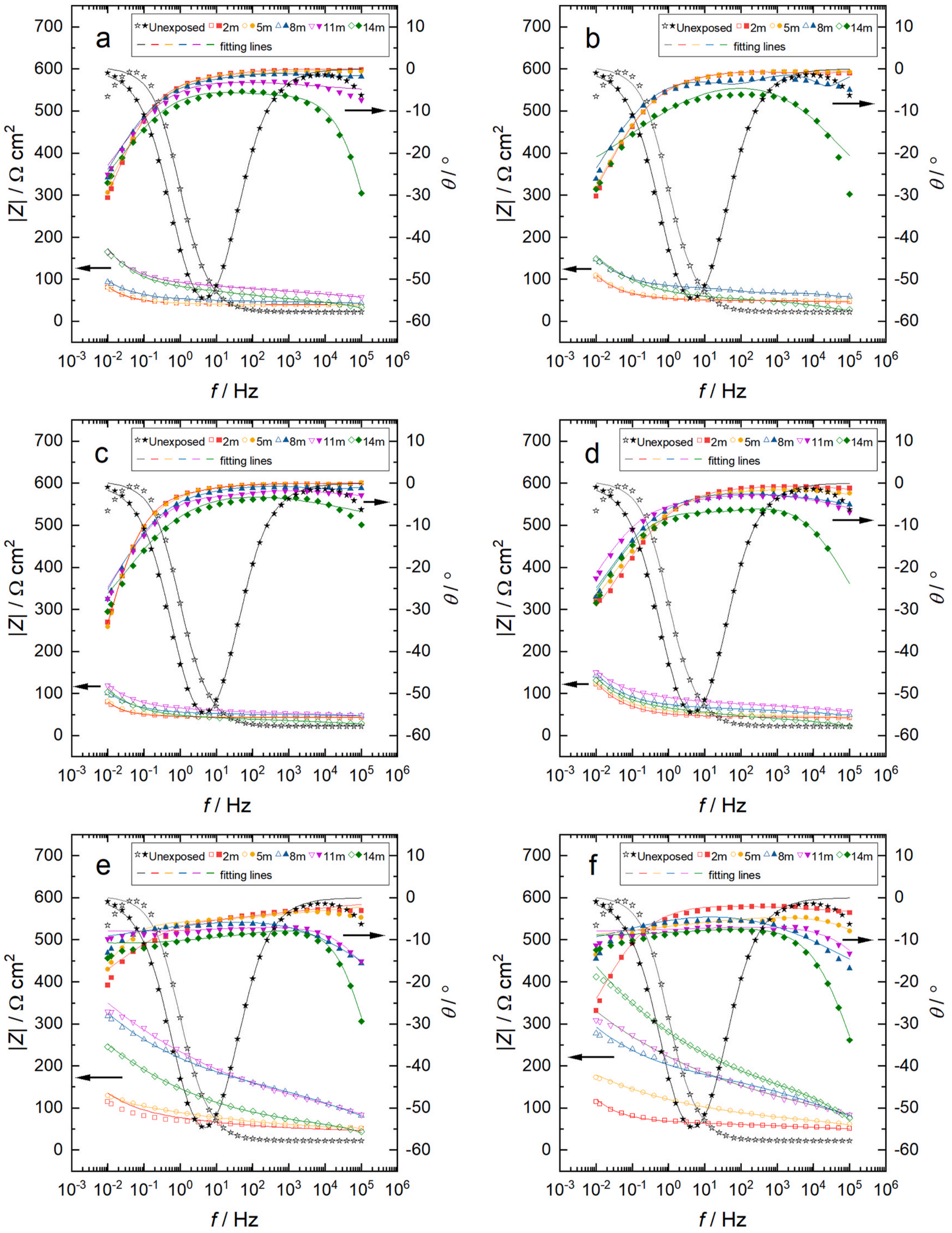

Fig. 11. Bode phase angle (θ vs. f) and impedance modulus ($|Z|$ vs. f) plots at OCP for unexposed and corroded S235 carbon steel in a 3.5 wt% NaCl solution. Exposure locations: **(a)** AM, **(b)** LM, **(c)** MA, **(d)** RG, **(e)** FG and **(f)** FV.

of the diffusion layer, a different mechanism, based on anomalous diffusion, occurs when species are influenced by the boundary (metallic interface). The species undergoing anomalous diffusion, do not move linearly with time but rather follow a power-law behaviour [49]. A characteristic frequency further divides the low frequency impedance plot into a lower and higher frequency region, with Warburg impedance appearing in the high region. The shape of the spectra in the low region is determined by the behaviour of the diffusing species on reaching the metallic interface. Above the characteristic frequency, the species do not travel far enough to cover the whole layer thickness, which gives rise to a semi-infinite behaviour (not affected by any conditions at the boundary) as observed in the case of FV and FG.

The Randles equivalent circuit does not reflect the complexity of the corrosive reaction due to the appearance of at least two time-constants caused by the corrosion layer [50]. Therefore, a charge transfer resistance (R_{ct}) and a CPE of non-ideal capacitive behaviour (CPE_1) is added, accompanied with the durability of the corrosion product layer. The latter comprises of the resistance and non-ideal capacitance of the rust layer (R_r and CPE_2). Changes in CPE behaviour can also arise due to increased surface roughness associated with a corroded surface and

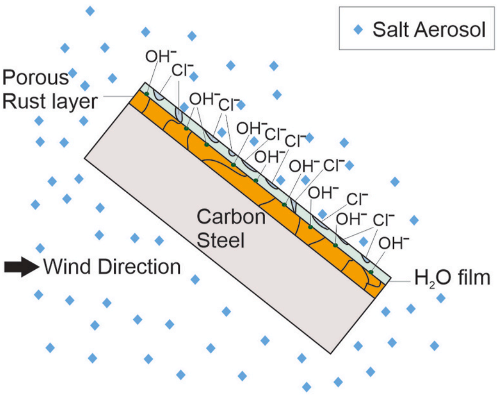

Fig. 12. Effect of hydroxides and chlorides on anodic dissolution.

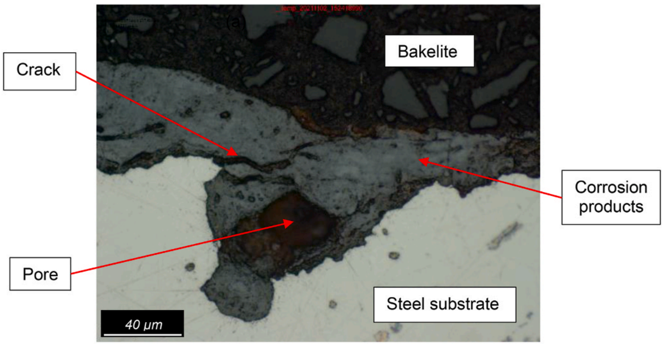

Fig. 13. Cross-sectional morphology of 14-month exposed plate at FG.

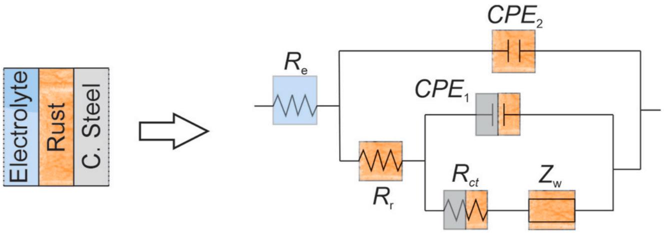

Fig. 14. Equivalent circuit for corrosion of the rust covered plates.

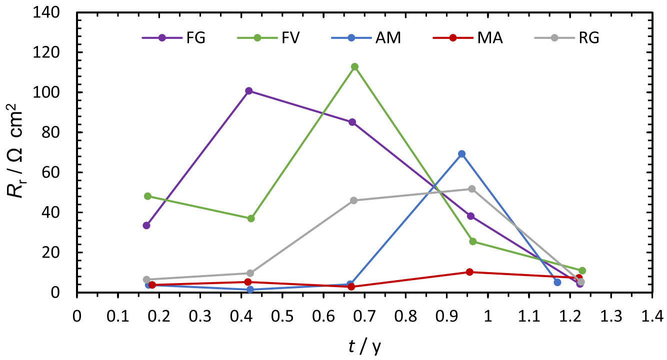

Fig. 15. Time Evolution of Rust Resistance (R_r), determined from EIS data fitted using the equivalent circuit of Fig. 14.

polymorphism of the oxide film in a direction normal to the surface [47]. The equivalent circuit is shown in Fig. 14 and similar models have been found to be appropriate for corroded carbon steel, as well as weathering steel, from various studies in the past [29,37,51]. The Warburg impedance component, Z_w, is added for AM, LM, RG and the later stages at MA given the diagonal line at low frequency in the Nyquist plot is close to 45°. The fitted lines are shown in Figs. 10 and 11, with the complete fitting data tabulated in the Appendix. The lower n_1 values after 14 months of exposure at AM, LM, MA and RG implies a significant increase in heterogeneity of the corroded surface. Since FV and FG were exposed to more aggressive atmospheric conditions, greater surface heterogeneity is likely to have occurred earlier leading to multiple time constants. The results obtained in this study demonstrates the porosity of the rust layer, implying that the associated resistance is determined by the number and size of the pores present and the value of the circuit component would be an indication of the morphology of the corrosion layer formed at the various locations, from which the protective ability can be deduced.

Fig. 15 shows R_r against exposure time and demonstrates significantly higher resistance of the rust layer at the FV and FG locations compared to the other sites throughout almost the entire first year of exposure. Given the relatively high corrosion rates at these two sites, the fast growth of the corrosion layer with consequently a higher proportion of stable rust phases (mainly goethite) [39] have probably led to the increased resistance. However, as observed across all sites, there is a significant drop which follows the marked increase in R_r, towards the end of the exposure period. This confirms formation of porous surface films leading to a highly permeable rust layer. This inherent protection against corrosion is therefore not effective and corroborates with the exponent *b* obtained for RG, MA and AM, which is close to the threshold of 0.5, beyond which indicates low corrosion performance. After 14 months of exposure, the *b* parameter still shows a more protective corrosion layer at FV and FG. However, the trend in the value of R_r implies that there is likely to be eventual acceleration of corrosion at these two locations due to widening of the pores caused by cracks in the rust layer. It should be noted that Fig. 15 does not include LM given unavailability of the data for 11-months at this site.

S235 being a ferrite-pearlite steel, the cementite (Fe_3C) from the metastable alternating ferrite and cementite lamella platelet structure of pearlite is detrimental to its corrosion resistance since ferrite and cementite form anodic and cathodic sites, respectively [52]. Cementite being insoluble, it is ferrite which undergoes dissolution. As corrosion proceeds, there is a formation and growth of the rust layer which covers the surface leaving the area of cementite exposed. This leads to a porous layer which is not sufficiently protective, eventually giving rise to a micro-galvanic effect. There is continuous reaction of the ferrite phase, dissolving preferentially, which explains the ineffectiveness of the corrosion layer as a protection. Furthermore, the non-uniform surface corrosion causes an increase in surface area leading to higher water retention ability [53]. This is more evident in the early stages of exposure at the various sites, with an acceleration of corrosion at AM, LM, MA and RG and to a higher extent at FG and FV, both being in proximity to a power plant and the sea, therefore exposed to aggressive species such as SO_2 and Cl^-. A schematic describing the general evolution of the rust layer is shown in Fig. 16. Build-up of corrosion layers can be considered to occur in four steps.

4. Conclusions

A combination of atmospheric exposures and *ex situ* electrochemical testing led to an in-depth understanding of the evolution and formation mechanism of the corrosion layer of S235 carbon steel subjected to a 14-months atmospheric exposure under various conditions within Port-Louis city. The main conclusions are as follows:

- Potentiodynamic polarization results showed that the cathodic reaction rate is much higher for the corroded samples than for the unexposed steel. This is associated to the formation of porous surface layers due to a micro-galvanic action occurring with the cementite and ferrite of the ferrite-pearlite steel, which resulted in a continuous

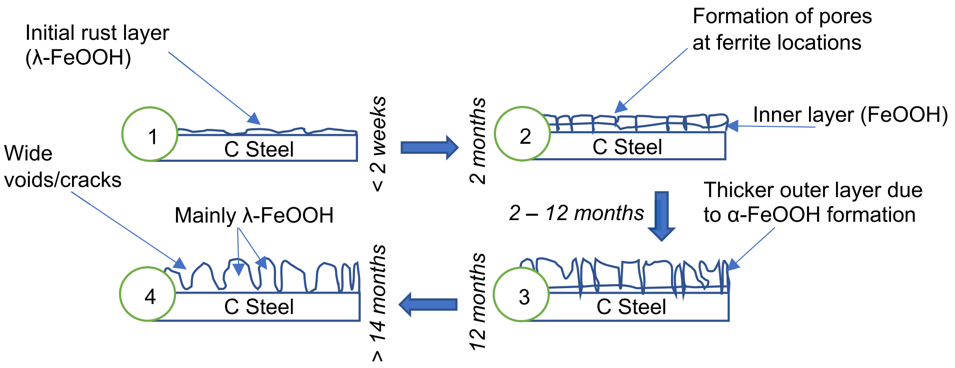

Fig. 16. Schematic illustration of rust layer evolution with details of oxide phase transformation.

anodic dissolution with time as oxygen and corrosion products are being reduced. Such a phenomenon occurs with a finite thickness of the rust layers, evident in the early months of exposure when the corrosion products accumulation on the surface is minimal.

- The low level of Cl$^-$ and SO$_2$ (7.8 and 1.2 mg m^{-2} d^{-1}, respectively) in the atmosphere, linked with the quieter waters of the bay (low marine aerosol production) and being further away from the main pollution sources, create the least aggressive atmosphere at MA. This corroborates well with the EIS results for this location which shows small size of the diffusion tail in the Nyquist plot. Therefore, this study shows that such a diffusion-controlled corrosion process is impacted by the concentration of ions such as chloride and sulphate.
- There are marked differences in corrosion mechanisms in a nominally similar urban environment (i.e., Port-Louis and within a 2 km radius). All processes are diffusion controlled, but with occurrence of anomalous diffusion for the more corroded samples, indicating existence of larger voids/cracks, and normal diffusion for milder sites, due to formation of a relatively compact rust. This increased understanding of geospatial corrosion behaviour is essential for material or corrosion protection method selection based on location in the city.
- Rust layer resistance (R_r), obtained from EIS performed on the corroded surfaces, can be used to track the time evolution of corrosion products, and reflects the varying corrosion kinetics observed across Port-Louis. A general decrease in R_r values to 4–10 Ω cm^2 towards the end of the exposure period signifies similar properties of the rust layers after 14 months. Further investigation beyond this period is required as the corrosion rate is expected to increase again without any significant protection from the rust layer.
- The XRD spectra indicate predominance of the lepidocrocite rust phase across all sites after 14 months of exposure, confirming humidity as the major factor driving corrosion processes in the region. Port-Louis is protected against incoming marine aerosols blown by the South-East winds, the mountain range being an effective barrier. However, corrosion rates many still rise significantly in areas affected by deposition of plumes coming from the flue-gas stacks.

Funding

This research did not receive any specific grant from funding agencies in the public, commercial, or not-for-profit sectors.

CRediT authorship contribution statement

Yashwantraj Seechurn: Conceptualization, Methodology, Formal analysis, Investigation, Writing – original draft, Writing – review & editing, Visualization. **Julian A. Wharton:** Writing – review & editing, Supervision. **Baboo Y.R. Surnam:** Supervision.

Declaration of competing interest

The authors declare that they have no known competing financial interests or personal relationships that could have appeared to influence the work reported in this paper.

Data availability

The raw/processed data required to reproduce these findings cannot be shared at this time as the data also forms part of an ongoing study.

Acknowledgements

The authors express their gratitude to the Central Electricity Board, Mauritius Civil Service Mutual Aid Association Ltd, Rajiv Gandhi Science Centre, Landscope Mauritius and ABC Motors for allocating the required space in their premises for the field tests.

Appendix A. Supplementary data

Supplementary data to this article can be found online at https://doi.org/10.1016/j.matchemphys.2022.126694.

References

[1] I. Matsushima, Carbon steel—atmospheric corrosion, in: R.W. Revie (Ed.), Uhlig's Corros. Handb, third ed., John Wiley & Sons, Inc., Hoboken, New Jersey, 2011, pp. 579–588, https://doi.org/10.1002/9780470872864.

[2] J.G. Castaño, C.A. Botero, A.H. Restrepo, E.A. Agudelo, E. Correa, F. Echeverría, Atmospheric corrosion of carbon steel in Colombia, Corros. Sci. 52 (2010) 216–223, https://doi.org/10.1016/j.corsci.2009.09.006.

[3] E. Del Angel, R. Vera, F. Corvo, Atmospheric corrosion of galvanised steel in different environments in Chile and Mexico, Int. J. Electrochem. Sci. 10 (2015) 7985–8004.

[4] J.C. Guerra, A. Castañeda, F. Corvo, J.J. Howland, J. Rodríguez, Atmospheric corrosion of low carbon steel in a coastal zone of Ecuador: anomalous behavior of chloride deposition versus distance from the sea, Mater. Corros. 70 (2019) 444–460, https://doi.org/10.1002/maco.201810442.

[5] F. Corvo, C. Haces, N. Betancourt, L. Maldonado, L. Véleva, M. Echeverria, O.T. De Rincón, A. Rincón, Atmospheric corrosivity in the Caribbean area, Corros. Sci. 39 (1997) 823–833, https://doi.org/10.1016/S0010-938X(96)00138-2.

[6] F. Corvo, T. Perez, L.R. Dzib, Y. Martin, A. Castañeda, E. Gonzalez, J. Perez, Outdoor-indoor corrosion of metals in tropical coastal atmospheres, Corros. Sci. 50 (2008) 220–230, https://doi.org/10.1016/j.corsci.2007.06.011.

[7] R. Vera, O.T. de Rincón, M. Bagnara, N. Romero, R. Araya, S. Ossandón, Tropical/non-tropical marine environments impact on the behaviour of carbon steel and galvanised steel, Mater. Corros. 69 (2018) 614–625, https://doi.org/10.1002/maco.201709873.

[8] Y. Ma, Y. Li, F. Wang, The atmospheric corrosion kinetics of low carbon steel in a tropical marine environment, Corros. Sci. 52 (2010) 1796–1800, https://doi.org/10.1016/j.corsci.2010.01.022.

[9] S.A. Abreu, P.F. Corvo, D. Ases, Use of anodic polarization curves to estimate rates of atmospheric corrosion and protective properties of corrosion products, Prot. Met. 18 (1982) 465–469.

[10] D. Landolt, Corrosion and Surface Chemistry metals.Pdf, EPFL Press, 2007.

[11] X. Zhang, S. Yang, W. Zhang, H. Guo, X. He, Influence of outer rust layers on corrosion of carbon steel and weathering steel during wet-dry cycles, Corros. Sci. 82 (2014) 165–172, https://doi.org/10.1016/j.corsci.2014.01.016.

[12] J. Wang, Z.Y. Wang, W. Ke, Corrosion behaviour of weathering steel in diluted Qinghai salt lake water in a laboratory accelerated test that involved cyclic wet/dry conditions, Mater. Chem. Phys. 124 (2010) 952–958, https://doi.org/10.1016/j.matchemphys.2010.07.069.

[13] Y. Zou, J. Wang, Y.Y. Zheng, Electrochemical techniques for determining corrosion rate of rusted steel in seawater, Corros. Sci. 53 (2011) 208–216, https://doi.org/10.1016/j.corsci.2010.09.011.

[14] J. Tkacz, J. Minda, S. Fintová, J. Wasserbauer, Comparison of electrochemical methods for the evaluation of cast AZ91 magnesium alloy, Materials 9 (2016) 43–48, https://doi.org/10.3390/ma9110925.

[15] J. Alcántara, D. de la Fuente, B. Chico, J. Simancas, I. Díaz, M. Morcillo, Marine atmospheric corrosion of carbon steel: a review, Materials 10 (2017), https://doi.org/10.3390/ma10040406.

[16] I.S. Cole, D. Lau, D.A. Paterson, Holistic model for atmospheric corrosion Part 6 - from wet aerosol to salt deposit, Corros. Eng. Sci. Technol. 39 (2004) 209–218, https://doi.org/10.1179/147842204X2880.

[17] H. Kaesche, Corrosion of Metals: Physicochemical Principles and Current Problems, Springer-Verlag, Berlin Heidelberg New York, 2003, https://doi.org/10.1007/978-3-642-96038-3.

[18] C. Leygraf, Wallin, J. Tidblad, T.E. Graedel, Atmospheric Corrosion, 2ndEdition ed., 2016. Hoboken, New Jersey.

[19] Y. Liu, Z. Wang, Y. Wei, Influence of seawater on the carbon steel initial corrosion behavior, Int. J. Electrochem. Sci. 14 (2019) 1147–1162, https://doi.org/10.20964/2019.02.36.

[20] Climate of Mauritius - Mauritius Meteorological Services, (n.d.). http://metservice.intnet.mu/climate-services/climate-of-mauritius.php (accessed June 18, 2021).

[21] C.G. Staub, F.R. Stevens, P.R. Waylen, The geography of rainfall in Mauritius: modelling the relationship between annual and monthly rainfall and landscape characteristics on a small volcanic island, Appl. Geogr. 54 (2014) 222–234, https://doi.org/10.1016/j.apgeog.2014.08.008.

[22] BS EN ISO 9223, Corrosion of Metals and Alloys — Corrosivity of Atmospheres — Classification , Determination and Estimation, BSI Standards Limited, 2012.

[23] ISO 8565, Metals and Alloys — Atmospheric Corrosion Testing — General Requirements, 2011.

[24] BS EN ISO 8407, Corrosion of Metals and Alloys - Removal of Corrosion Products from Corrosion Test Specimens, BSI Standards Limited, 2014.

[25] BS EN ISO 9226, Corrosion of Metals and Alloys - Corrosivity of Atmospheres - Determination of Corrosion Rate of Standard Specimens for the Evaluation of Corrosivity, BSI Standards Limited, 2012.

[26] BS EN ISO 9224, Corrosion of Metals and Alloys — Corrosivity of Atmospheres — Guidance Values for the Corrosvity Categories, BSI Standards Limited, 2012.

[27] D. Xia, C. Ma, S. Song, L. Xu, Detection of atmospheric corrosion of aluminium alloys by electrochemical probes: theoretical analysis and experimental tests, J. Electrochem. Soc. 166 (2019) B1000–B1009, https://doi.org/10.1149/2.0871912jes.

[28] D. Xia, S. Song, Z. Qin, W. Hu, Y. Behnamian, Review-electrical probes and sensors designed for time-dependent atmospheric corrosion monitoring: fundamentals, progress and challenges, J. Electrochem. Soc. 167 (2020), 037513, https://doi.org/10.1149/2.0132003JES.

[29] J.J. Santana Rodríguez, F.J. Santana Hernández, J.E. González González, Mathematical and electro-chemical characterisation of the layer of corrosion products on carbon steel in various environments, Corros. Sci. 44 (2002) 2597–2610, https://doi.org/10.1016/S0010-938X(02)00048-3.

[30] P. Webb, Introduction to Oceanography: Estuaries, 2017, pp. 2001–2006. https://rwu.pressbooks.pub/webboceanography/chapter/13-6-estuaries/.

[31] A. Nishikata, F. Suzuki, T. Tsuru, Corrosion monitoring of nickel-containing steels in marine atmospheric environment, Corros. Sci. 47 (2005) 2578–2588, https://doi.org/10.1016/j.corsci.2004.10.009.

[32] B.Y.R. Surnam, C.V. Oleti, Atmospheric corrosion in Mauritius, Corros. Eng. Sci. Technol. 47 (2012) 446–455, https://doi.org/10.1179/1743278212Y.0000000026.

[33] Mauritius Meteorological Services, Meteorological Observations and Climatological Summaries, 2019. http://metservice.intnet.mu/publication.php.

[34] J.F. Ríos Rojas, D. Escobar Ocampo, E.A. Hernández García, C.E. Arroyave Posada, Atmospheric corrosivity in Bogota as a very high-altitude metropolis questions international standards, Dyna 82 (2015) 128–137, https://doi.org/10.15446/dyna.v82n190.46256.

[35] C. Pan, W. Han, Z. Wang, C. Wang, G. Yu, Evolution of initial atmospheric corrosion of carbon steel in an industrial atmosphere, J. Mater. Eng. Perform. 25 (2016) 5382–5390, https://doi.org/10.1007/s11665-016-2312-0.

[36] C.M.A. Brett, I.A.R. Gomes, J.P.S. Martins, Inhibition of aluminium corrosion in chloride media: an impedance study, J. Appl. Electrochem. 24 (1994) 1158–1163, https://doi.org/10.1007/BF00241315.

[37] W. Wu, X. Cheng, J. Zhao, X. Li, Benefit of the corrosion product film formed on a new weathering steel containing 3% nickel under marine atmosphere in Maldives, Corros. Sci. 165 (2020), 108416, https://doi.org/10.1016/j.corsci.2019.108416.

[38] W. Chen, L. Hao, J. Dong, W. Ke, Effect of sulphur dioxide on the corrosion of a low alloy steel in simulated coastal industrial atmosphere, Corros. Sci. 83 (2014) 155–163, https://doi.org/10.1016/j.corsci.2014.02.010.

[39] Y. Seechurn, B.Y.R. Surnam, J.A. Wharton, Marine atmospheric corrosion of carbon steel in the tropical microclimate of Port Louis, Mater. Corros. (2022), https://doi.org/10.1002/maco.202112871.

[40] N. Mahato, M.M. Singh, Investigation of passive film properties and pitting resistance of AISI 316 in aqueous ethanoic acid containing chloride ions using electrochemical investigation of passive film properties and pitting resistance of AISI 316 in aqueous ethanoic acid contai, Port. Electrochim. Acta 29 (2011) 233–251, https://doi.org/10.4152/pea.201104233.

[41] D. Klotz, Negative capacitance or inductive loop? – a general assessment of a common low frequency impedance feature, Electrochem. Commun. 98 (2019) 58–62, https://doi.org/10.1016/j.elecom.2018.11.017.

[42] D. Xia, C. Deng, D. Macdonald, S. Jamali, D. Mills, J. Luo, M.G. Strebl, M. Amiri, W. Jin, S. Song, W. H, Electrochemical measurements used for assessment of corrosion and protection of metallic materials in the field: a critical review, J. Mater. Sci. Technol. 112 (2022) 151–183, https://doi.org/10.1016/j.jmst.2021.11.004.

[43] Q.X. Li, Z.Y. Wang, W. Han, E.H. Han, Characterization of the rust formed on weathering steel exposed to Qinghai salt lake atmosphere, Corros. Sci. 50 (2008) 365–371, https://doi.org/10.1016/j.corsci.2007.06.020.

[44] V. Encinas-Sánchez, M.T. de Miguel, M.I. Lasanta, G. García-Martín, F.J. Pérez, Electrochemical impedance spectroscopy (EIS): an efficient technique for monitoring corrosion processes in molten salt environments in CSP applications, Sol. Energy Mater. Sol. Cells 191 (2019) 157–163, https://doi.org/10.1016/j.solmat.2018.11.007.

[45] T. Nishimura, Electrochemical behaviour and structure of rust formed on Si- and Al-bearing steel after atmospheric exposure, Corros. Sci. 52 (2010) 3609–3614, https://doi.org/10.1016/j.corsci.2010.07.006.

[46] A. Anderko, Modeling of aqueous corrosion, in: B. Cottis, M. Graham, R. Lindsay, S. Lyon, T. Richardson, D. Scantlebury, H. Stott (Eds.), Shreir's Corros, Elsevier, Amsterdam, 2010, pp. 1585–1629.

[47] M.E. Orazem, B. Tribollet, Electrochemical Impedance Spectroscopy, second ed., John Wiley & Sons, Inc., Hoboken, New Jersey, 2017.

[48] O.E. Barcia, E. D'Elia, I. Frateur, O.R. Mattos, N. Pébère, B. Tribollet, Application of the impedance model of de Levie for the characterization of porous electrodes, Electrochim. Acta 47 (2002) 2109–2116, https://doi.org/10.1016/S0013-4686(02)00081-6.

[49] J. Bisquert, A. Compte, Theory of the electrochemical impedance of anomalous diffusion, J. Electroanal. Chem. 499 (2001) 112–120, https://doi.org/10.1016/S0022-0728(00)00497-6.

[50] A.N. Ababneh, M.A. Sheban, M.A. Abu-Dalo, Effectiveness of benzotriazole as corrosion protection material for steel reinforcement in concrete, J. Mater. Civ. Eng. 24 (2012) 141–151, https://doi.org/10.1061/(asce)mt.1943-5533.0000374.

[51] Y. Fan, W. Liu, S. Li, T. Chowwanonthapunya, B. Wongpat, Y. Zhao, B. Dong, T. Zhang, X. Li, Evolution of rust layers on carbon steel and weathering steel in high humidity and heat marine atmospheric corrosion, J. Mater. Sci. Technol. 39 (2020) 190–199, https://doi.org/10.1016/j.jmst.2019.07.054.

[52] X. Hao, J. Dong, I.I.N. Etim, J. Wei, W. Ke, Sustained effect of remaining cementite on the corrosion behavior of ferrite-pearlite steel under the simulated bottom plate environment of cargo oil tank, Corros. Sci. 110 (2016) 296–304, https://doi.org/10.1016/j.corsci.2016.04.042.

[53] H.U. Sajid, R. Kiran, Influence of corrosion and surface roughness on wettability of ASTM A36 steels, J. Constr. Steel Res. 144 (2018) 310–326, https://doi.org/10.1016/j.jcsr.2018.01.023.